Published in final edited form as:
Nat Med. 2014 July ; 20(7): 778–784. doi:10.1038/nm.3484.

On-demand intracellular amplification of chemoradiation with cancer-specific plasmonic nanobubbles

Ekaterina Y Lukianova-Hleb[1], **Xiaoyang Ren**[#2], **Rupa R Sawant**[#3], **Xiangwei Wu**[2], **Vladimir P Torchilin**[3], and **Dmitri O Lapotko**[1,4]

[1]Department of Biochemistry and Cell Biology, Rice University, Houston, Texas, USA

[2]Department of Clinical Cancer Prevention, University of Texas MD Anderson Cancer Center, Houston, Texas, USA

[3]Center for Pharmaceutical Biotechnology and Nanomedicine, Northeastern University, Boston, Massachusetts, USA

[4]Department of Physics and Astronomy, Rice University, Houston, Texas, USA

[#] These authors contributed equally to this work.

Abstract

Chemoradiation-resistant cancers limit treatment efficacy and safety. We show here the cancer cell–specific, on-demand intracellular amplification of chemotherapy and chemoradiation therapy via gold nanoparticle– and laser pulse–induced mechanical intracellular impact. Cancer aggressiveness promotes the clustering of drug nanocarriers and gold nanoparticles in cancer cells. This cluster, upon exposure to a laser pulse, generates a plasmonic nanobubble, the mechanical explosion that destroys the host cancer cell or ejects the drug into its cytoplasm by disrupting the liposome and endosome. The same cluster locally amplifies external X-rays. Intracellular synergy of the mechanical impact of plasmonic nanobubble, ejected drug and amplified X-rays improves the efficacy of standard chemoradiation in resistant and aggressive head and neck cancer by 100-fold *in vitro* and 17-fold *in vivo*, reduces the effective entry doses of drugs and X-rays to 2–6% of their clinical doses and efficiently spares normal cells. The developed quadrapeutics technology combines four clinically validated components and transforms a standard macrotherapy into an intracellular on-demand theranostic microtreatment with radically amplified therapeutic efficacy and specificity.

Correspondence should be addressed to D.O.L. (dl5@rice.edu).

Note: Any Supplementary Information and Source Data files are available in the online version of the paper.

AUTHOR CONTRIBUTIONS

E.Y.L.-H.,V.P.T. and D.O.L. discussed the results and wrote the paper; D.O.L. conceived the strategy and designed the experiments; E.Y.L.-H. and D.O.L. performed the experiments; E.Y.L.-H., V.P.T., X.W. and D.O.L. analyzed the data; R.R.S. prepared nanocarriers; and X.W. and X.R. prepared and analyzed the animals.

COMPETING FINANCIAL INTERESTS

The authors declare no competing financial interests.

The drug and radiation resistance and aggressiveness of some cancers (head and neck, brain, prostate, lung and others) result in their high lethality, especially when doses of current therapies are limited by their high nonspecific toxicity. Surgery often cannot fully resect such tumors if they are intertwined with important normal tissues, and incomplete tumor resection results in dangerous microscopic residual disease (MRD)[1]. Inability to safely resect or treat such aggressive cancers ultimately reduces patient survival rates and quality of life[2]. Therefore, it is highly desirable to develop a new approach that (i) selectively amplifies the efficacy of standard therapies only in cancer cells, (ii) preserves the functionality of colocalized normal tissues and (iii) reduces nonspecific toxicity and treatment time.

We achieved this goal through the intracellular amplification of chemotherapy and radiation therapy by employing intracellular synergy of four clinically validated components (Fig. 1): encapsulated drugs, colloidal gold nanoparticles (GNPs)[3,4], near-infrared short laser pulses and X-rays in a new method we termed quadrapeutics. We hypothesized that the administration and activation of these four components in a simple protocol would initiate several new therapeutic mechanisms inside cancer cells (Fig. 1). First, the cells would self-assemble systemically administered antibody-functionalized GNPs and drug-loaded nanocarriers into intracellular nanoclusters via receptor-mediated endocytosis. Second, the on-demand threshold activation of these nanoclusters with locally administered laser pulse and X-rays would trigger colocalized intracellular therapeutic events: the mechanical impact of vapor plasmonic nanobubbles (PNBs), instantaneous ejection of drugs into cytoplasm from PNB-disrupted nanocarriers and local amplification of X-rays. The intracellular synergy of these three threshold-activated, mechanical and physical transient events would selectively amplify the therapeutic effect of standard chemoradiation only in cancer cells.

We evaluated quadrapeutics for an aggressive and resistant cancer, using head and neck squamous cell carcinoma (HNSCC) as a model, with clinically validated gold colloids, encapsulated doxorubicin and paclitaxel, picosecond laser pulses and X-rays both *in vitro* and *in vivo*.

RESULTS

PNB-induced ejection of an encapsulated payload

We studied PNB-induced ejection (release) of an encapsulated payload in the HNSCC HN31 cell line (Fig. 2). We concurrently targeted cancer cells by using a clinically validated target, epidermal growth factor receptor (EGFR), with a C225 antibody[5] conjugated to 60-nm solid GNPs and by using liposomal green fluorescent dye conjugated to 2C5 antibody[6]. A high level of EGFR expression resulted in the endocytotic formation of intracellular GNP-liposome clusters that revealed optical scattering of GNPs (Fig. 2a) but showed no fluorescence owing to its quenching in intact liposomes (Fig. 2a). Next, we exposed the cells to a single picosecond laser pulse of the low fluence of 40 mJ cm^{-2} at 532 nm. We simultaneously detected PNBs optically with the laser pulse (Fig. 2b). The PNB location in cells coincided with that of the GNP cluster (Fig. 2b), and the PNB's optical trace showed PNB expansion and collapse within 50–60 ns (Fig. 2b). The duration of the trace, the PNB lifetime, characterized its maximal diameter[7]. Immediately after the PNB generation,

reimaged cells yielded a bright liposome-specific green fluorescence in submicrometer zones colocalized with the GNP clusters and PNBs (Fig. 2c). We observed no released dye in PNB-negative cells (data not shown). Three-dimensional confocal images of the cells confirmed dye release into the cellular cytoplasm (Supplementary Fig. 1). The small maximal size of the PNB (200–400 nm for a PNB with a 60-ns lifetime[7]) and its mechanical, not thermal, nature[7] coupled with the high speed of the PNB expansion (30 ns) and dye ejection resulted in a high intracellular dye concentration and localization. We quantified this via image cytometry of the PNB-treated cells (Fig. 2d).

We studied the cancer cell specificity of the PNB-induced payload release mechanism in a mixed suspension of EGFR-positive HN31 cells and EGFR-negative suspension-stable human J32 cells. We mixed the cells and treated them identically with the conjugates of GNPs and liposomal green dye, as in the previous experiment, and obtained tricolor images of the mixed suspension (Fig. 2e). A broad laser pulse (532 nm, 40 mJ cm^{-2}) simultaneously irradiated hundreds of mixed cells. We observed PNBs with a lifetime of 55–60 ns in HN31 but none in J32 cells (Fig. 2f). The threshold nature of PNBs[7] prevented their generation in EGFR-negative cells, as these cells did not form sufficiently large GNP clusters (Fig. 3h) and therefore had a PNB generation threshold fluence[8,9] above the level of the applied laser fluence (Supplementary Fig. 2). The second tricolor image, obtained immediately after laser treatment, revealed localized intracellular bright green fluorescence in HN31 cells but none in J32 cells (Fig. 2g). Image cytometry of 150–180 HN31 and J32 cells (Fig. 2h) showed (i) that the onset of local green fluorescence coincided with PNB generation, (ii) a high intracellular localization of the released payload and (iii) high cancer cell specificity of the PNB-induced release (ejection) of the liposomal payload.

Therapeutic responses to single and combination treatments

We analyzed short- and long-term therapeutic effects *in vitro*. We used liposomal doxorubicin (Doxil, Ben Venue Laboratories) and micellar paclitaxel as drug nanocarriers[10,11]. These nanocarriers alone had revealed low cancer cell specificity and revealed the high drug resistance of HN31 cells (Fig. 3a). PNBs alone revealed the cancer cell–specific therapeutic effect only at the high laser fluence associated with large PNBs that cause cell mechanical disruption[12] and have more than a 200-ns lifetime; smaller PNBs were nonlethal (Fig. 3b). In contrast, the colocalization of small PNBs with drug nanocarriers in cancer cells significantly improved the therapeutic efficacy (Fig. 3d), especially in the short term (Supplementary Fig. 3a,b). Thus, PNB-induced intracellular release of soluble doxorubicin and insoluble paclitaxel amplified both the efficacy and specificity of chemotherapy. At the same time, the absence of PNBs in normal cells coupled with entry drug doses reduced to 2–3% of their standard dose effectively spared normal cells under identical treatment (Fig. 3e and Supplementary Fig. 3a,b). However, this therapeutic amplification requires effective intracellular colocalization of the drug nanocarriers and PNBs. Without such colocalization, the mechanical impact of PNBs did not reach the otherwise randomly internalized drug nanocarriers, resulting in a relatively poor therapeutic effect (Supplementary Fig. 3c,d).

X-rays alone without drugs and GNPs were efficient only at high and unsafe doses due to the radiation resistance of HN31 cells (Fig. 3c). GNPs improved the therapeutic efficacy of X-rays via the emission of local secondary electrons[13,14] but only incrementally (Fig. 3d and Supplementary Fig. 3e). The combination of X-rays and therapeutic nanocarriers resulted in a predictable therapeutic effect (Fig. 3d and Supplementary Fig. 3e) owing to the well-known synergy of drugs and X-rays[15,16]. To summarize, neither the tested therapeutic components alone, nor their standard combinations described above, prevented the growth of resistant and aggressive cancer cells.

In contrast, the administration of all four components as quadrapeutics resulted in a radical amplification of therapeutic efficacy (Fig. 3d) and specificity (Fig. 3e). We achieved an even stronger effect, the full suppression of cancer cell proliferation, when we applied X-rays 6 h after PNB treatment (Fig. 3d). Identically treated normal cells demonstrated high long- and short-term viability (Fig. 3e and Supplementary Fig. 3f).

Nanoclusters and PNBs in therapeutic amplification

We studied the role of nanoclusters and PNBs in therapeutic amplification by analyzing therapeutic responses, GNP and PNB size in normal epithelial (NOM9) cells, slow-growing indolent HNSCC[17] (HN30) cells and fast-growing aggressive HNSCC[17] (HN31) cells, all identically treated with quadrapeutics and standard chemoradiation. Compared to indolent cells, aggressive cells were more resistant to standard chemoradiation (Fig. 3f). In contrast, they could not resist quadrapeutics, which completely suppressed their growth.

We quantified the therapeutic amplification with cancer aggressiveness by dividing the surviving fractions of chemoradiation-treated cells with those of quadrapeutics-treated cells. This therapeutic amplification coefficient has been analyzed as the function of the growth rate of intact xenograft tumors in mice induced with specific cancer cell lines (Fig. 3g). The therapeutic amplification coefficient rapidly increased above 100 for aggressive HN31 cells, thus revealing the self-regulation of therapeutic efficacy with cancer aggressiveness. This amplification coefficient correlated with the size of the intracellular GNP nanoclusters and PNBs (Fig. 3g): normal cells nonspecifically internalized single GNPs (Fig. 3h) with the high PNB generation threshold fluence and therefore did not generate PNBs. Thus, normal cells survived the treatment (Fig. 3f); indolent HN30 cells formed medium nanoclusters (Fig. 3i) with the lower PNB generation threshold fluence and thus generated very small PNBs, resulting in a moderate therapeutic amplification; and aggressive HN31 cells formed the largest nanoclusters (Fig. 3j) with the lowest PNB generation threshold fluence and thus generated maximal PNBs, resulting in the maximal therapeutic amplification.

These experiments reveal quadrapeutics' unique combination of cancer cell–specific multifold therapeutic amplification of low entry doses of drugs (2–3% of their standard does) and X-rays (6–7%) and a radical reduction in nonspecific toxicity.

Evaluation of quadrapeutics *in vivo*

To evaluate quadrapeutics *in vivo*, we used HNSCC as a model. We studied the basic mechanisms of quadrapeutics in primary HNSCC (Fig. 4) and evaluated its translational

potential for intraoperative theranostics (detection and treatment) of MRD[1], a highly aggressive and lethal disease that represents one of the major challenges of HNSCC treatment (Fig. 5).

We first analyzed the efficacy of the systemic delivery of GNPs and of local PNB generation and detection in a mouse model using HN31 cells. The systemic administration of C225-conjugated GNPs (0.8 μg g^{-1} body weight) resulted, after 24 h, in large GNP clusters in tumors (Supplementary Fig. 4a), whereas the normal adjacent tissue showed only single unclustered GNPs (Supplementary Fig. 4b,c), similar to *in vitro* results. Exposure of a tumor to a single broad near-infrared laser pulse (780 nm, 45 mJ cm^{-2}) resulted in generation of PNBs, which were detected *in vivo* via acoustic traces (Fig. 5a and Supplementary Fig. 5a); we used trace amplitude as a metric of a PNB[18]. *In vivo* PNBs revealed high cancer cell sensitivity and specificity (Supplementary Fig. 5b), low toxicity and high spectral selectivity[18] (Supplementary Fig. 5c).

Next, we evaluated the therapeutic efficacy of quadrapeutics against primary HNSCC tumors in two mouse models. In the first model, we injected a low number of pretreated HN31 cells subcutaneously into the flanks of mice and monitored the tumor growth (Fig. 4a–c). We compared four groups: intact cells, cells treated with PNBs (55-ns lifetime) alone, cells treated with chemoradiation (Doxil (2 μg ml^{-1}) and X-rays (4 Gy)) and cells treated with quadrapeutics (Doxil-C225, 2 μg ml^{-1}; GNP-C225, 2.4×10^{10} GNP ml^{-1}; laser pulse, 780 nm, 45 mJ cm^{-2} at 24 h after GNP and drug administration; and X-rays, 4 Gy, 6 h after laser treatment). After 15 d, tumors in the animals injected with intact cells reached moribund condition (Fig. 4a,c). Similarly, we observed large tumors after treatment with small PNBs alone (Fig. 4a). Standard chemoradiation also did not prevent tumor growth (Fig. 4b). In contrast, in the quadrapeutics-treated group, we found no or very small tumors (Fig. 4b,c), with tumor volumes less than 5% of those observed in the chemoradiation-treated group (Fig. 4c).

In the second model, we induced primary tumors with HN31 cells expressing luciferase. We compared the therapeutic response to a single treatment *in vivo* among four groups: the quadrapeutics group (GNP-C225, 0.8 μg per g body weight (μg g^{-1}) and Doxil-C225, 1 mg per kg body weight (mg kg^{-1}) systemically; laser pulse, 780 nm, 45 mJ cm^{-2} in 24 h; and X-rays (4 Gy) in 6 h), the chemoradiation group (same doses of drug and X-rays), the PNB group (same doses of GNPs and laser pulses) and the control group (no treatment). After a single treatment, we monitored all animals weekly for tumor volumes and bioluminescence (Fig. 4d–g). The quadrapeutics treatment rapidly suppressed tumor growth after the first week (Fig. 4e,g) to 3% of that in the control group and to 6% of that in the chemoradiation group (Fig. 4f). Small PNBs alone or chemoradiation alone did not prevent tumor growth and demonstrated relatively low therapeutic efficacy (Fig. 4g). In contrast, quadrapeutics radically accelerated and improved the effect of chemoradiation by 17-fold by 1 week after a single administration (Fig. 4g).

Next, we evaluated the translational potential of quadrapeutics for an intraoperative diagnosis and adjuvant treatment of MRD. We grew a primary HNSCC tumor from HN31 cells. We administered GNP and Doxil conjugates systemically, as described above, 24 h

before the tumor resection. Immediately after resecting the tumor, we scanned the surgical margins for 20–30 s with a broad near-infrared pulsed laser (780 nm, 45 mJ cm^{-2}, Fig. 5a). We simultaneously detected PNBs acoustically during the laser scan by using an ultrasound sensor (Fig. 5a and Supplementary Fig. 5a). We compared the amplitudes of PNB acoustical traces for the primary tumor, surgical margins and adjacent muscle tissues in GNP-treated and intact animals (Fig. 5b). The PNBs detected in surgical margins indicated the presence of MRD (Fig. 5b), as later confirmed by local tumor recurrences. At the same time, standard photoacoustic imaging of the same animals was unable to detect even the large primary tumor (Supplementary Fig. 5d). This experiment demonstrated the high HNSCC sensitivity and specificity and high speed of the PNB-based intraoperative diagnosis of MRD in a biopsy-free and real-time manner.

Intraoperative adjuvant treatment

We analyzed the intraoperative adjuvant treatment of MRD for three groups: surgery, surgery with chemoradiation (Doxil, 1 mg kg^{-1}, 24 h before surgery, and X-rays, 4 Gy, 6 h after surgery) and surgery with quadrapeutics (Doxil, 1 mg kg^{-1} concomitantly with GNPs (0.8 μg g^{-1}), 24 h before surgery, laser scan during surgery (780 nm, 45 mJ cm^{-2}) and X-rays, 4 Gy, 6 h after surgery). We confirmed the presence of MRD intraoperatively via PNB acoustic signals immediately after the tumor resection as described above.

Monitoring of local recurrence of HNSCC after treatment revealed that surgery alone resulted in tumor recurrence in 2–4 weeks in 100% of the animals (Fig. 5a,f) and that surgery with adjuvant chemoradiation also failed to prevent tumor recurrence (Fig. 5d,f). In contrast, surgery with adjuvant quadrapeutics efficiently suppressed tumor recurrence (Fig. 5e,f). Thus, quadrapeutics provided efficient intraoperative detection and treatment of MRD in a single theranostic (diagnosis and treatment) procedure.

DISCUSSION

The quadrapeutics paradigm lies in the cancer cell–specific intracellular synergistic amplification of standard macrotherapies by their conversion into combination microtherapy. The high therapeutic efficacy, the cancer cell specificity, the speed and the low nonspecific toxicity of quadrapeutics are achieved via the formation and on-demand threshold activation of intracellular nanoclusters of GNPs and drug nanocarriers, which remain safe and stable until activated with a laser pulse and X-rays. Nanocluster size increases with the cancer aggressiveness, and it is this size that, in turn, determines the threshold activation laser energy and the therapeutic efficacy of the four quadrapeutics components which, taken alone, are safe *in vitro* and *in vivo*. Thus, an intracellular nanocluster serves as a kind of ‘Trojan horse’, whose activation threshold energy decreases with size and thus makes it possible to selectively trigger the two on-demand therapeutic events only in cancer cells that self-assemble the largest nanoclusters.

The first event is the intracellular mechanical (nonthermal) impact of the laser pulse–induced PNB expansion and collapse around the laser pulse–heated GNP nanocluster. A PNB is not a particle but rather a transient nonstationary event lasting nanoseconds that mechanically disrupts a host cell (large PNB), colocalized nanocarriers and endosomes

(small sublethal PNB), causing them to locally and instantaneously eject the drug into the cytoplasm and thus create high intracellular concentration of the drug. A near-infrared laser pulse of low energy safely penetrates deep into tissue[19] or can be delivered to specific organs with standard optical catheters and endoscopes[20,21]. The largest nanoclusters, which form in aggressive cancer cells, require minimal laser energy to generate the large, lethal PNBs[7,18,22]. Smaller, nonspecific nanoclusters or even single GNPs nonspecifically internalized by normal cells require a much higher level of laser energy (fluence) for PNB generation, thereby preventing PNBs from being generated with an identical laser pulse[8,9,22]. The slow diffusive release of the drug from few nonspecifically internalized nanocarriers in normal cells does not induce notable nonspecific toxicity especially under radically reduced drug doses used by quadrapeutics.

The second event is the intracellular amplification of X-rays. This amplification, which occurs through the local emission of secondary electrons[13] by GNP nanoclusters upon absorption of external X-rays, is maximal around the largest nanoclusters. GNPs alone enhance radiotherapy[13,23], but they do so at the cost of high GNP doses. At lower safe GNP doses, the therapeutic gain is low. GNPs can also carry a drug and then amplify X-rays[24], but in the absence of the intracellular colocalization of the released drug and amplified X-rays, no synergistic amplification of their therapeutic effect occurs.

The synergy of the transient events described above (mechanical impact, drug ejection and X-ray amplification) is achieved via their intracellular colocalization, which radically amplifies their individual therapeutic effects. This amplification can be explained through well-established macroeffects: the mutual enhancement of chemotherapy and radiation therapy[16,25–27] and the mechanical radio- and chemosensitization of tumors[28–33]. However, it is the cancer cell–specific nanocluster that efficiently colocalizes the above therapeutic events and thus synergistically amplifies their therapeutic effect only in cancer cells. It is the nonstationary transient nanosecond nature of these events that efficiently confines their therapeutic impacts to the host cancer cell. This single cancer cell selectivity is impossible with standard therapies, which, in contrast, employ stationary materials and processes that still deliver macrotreatment even when using nanoparticles[34–36]. The therapeutic functions of quadrapeutics are complemented by the real-time diagnostic effect of PNBs. Emission of a pressure pulse by PNBs enables a rapid and highly sensitive diagnosis. Current intraoperative diagnostic methods require biopsy and are slow and often inaccurate[1,37]. Although the PNB method is technically close to photoacoustics[38], the latter, unlike PNBs, has low sensitivity owing to the weak acoustic emission by GNPs compared to that by PNBs. The acoustic detection of PNBs is also advantageous over optical intraoperative diagnostic methods[39], which are less sensitive and cancer cell specific.

To summarize, quadrapeutics technology converts established macrotherapies into an on-demand intracellular combination microtreatment. Cancer cell–specific GNP nanoclusters and PNBs accelerate and amplify the therapeutic efficacy and specificity of drugs and radiation up to 17-fold in highly resistant and aggressive tumors *in vivo* within a week after a single treatment. Cancer diagnosis and treatment are united into a single theranostic procedure, whose speed, sensitivity, specificity and efficacy enable the real-time intraoperative detection and treatment of MRD in head and neck cancer, reduce efficient

entry therapeutic doses of encapsulated drugs and X-rays to 2–6% of their standard doses, simplify the treatment and minimize its nonspecific toxicity.

ONLINE METHODS

Overview

Quadrapeutics is administered in three simple steps, each of which further amplifies the therapeutic efficacy and specificity (Supplementary Fig. 6): nanoparticle cluster formation, threshold activation of these nanoclusters with a single laser pulse for mechanical cell disruption and drug release and activation of these nanoclusters with X-rays for the local amplification of the X-ray dose by nanoclusters. These three steps described in detail below employ four therapeutic components: colloidal gold, drug-loaded nanocarriers, laser pulses and X-rays.

Step 1: nanoparticle cluster formation

Nanoparticle cluster formation (Supplementary Fig. 6a) via systemic administration of gold nanoparticles and therapeutic nanocarriers employed EGFR-specific antibody–conjugated 60-nm gold nanoparticles (GNPs) and therapeutic drug–loaded nanocarriers (TN). These GNPs are known as colloidal gold, the type of gold nanoparticles used in the clinic for more than 50 years[3,4,40,41]. They were conjugated with the clinically approved for HNSCC treatment antibodies against EGFR, Erbitux (ImClone Systems Inc., Branchburg, NJ) (C225)[5]. The use of gold colloids in near-infrared[18] as efficient PNB sources eliminated the need for specifically engineered near-infrared nanoparticles such as nanoshells or nanorods. The sterile GNP conjugates were prepared by BioAssayWorks LLC and VanPelt Bioescience LLC (Ijamsville, MD) and were administered at the concentration of 2.4×10^{10} NPs ml^{-1} *in vitro* and 0.8 μg g^{-1} of body weight *in vivo* (via intravenous injection) simultaneously with drug-loaded nanocarriers. We used three types of TNs that were not chemically linked to GNPs and were administered concurrently. This concomitant administration allows for administration of any type of encapsulated drug because GNPs and drug are not linked. Instead of Doxil, more traditional cisplatin (its liposomal analog Lipoplatin (Regulon Inc., Alimos, Greece)) can be used for HNSCC.

Calcein green–loaded liposomes—We employed calcein green–loaded liposomes to study the release process. Calcein green AM (C34852, Invitrogen, Carlsbad, CA) was encapsulated into liposomes that were 149 ± 23 nm and prepared by the lipid film hydration method. Liposomes were functionalized with 2C5 antibody raised against cancer-specific nucleosomes[6] and were incubated with cells simultaneously with GNP-C225 conjugates for 24 h (37 °C). The production and the purification of the mAb 2C5 were carried out by Harlan Bioproducts (Indianapolis, IL) using the cell line from our laboratory. Control IgG2a isotype-matching antibody clone UPC-10 was from Sigma. The optical absorbance of the calcein green dye at 532 nm was more than six orders of magnitude lower than that for GNPs, and given the low fluence of the laser pulse, the dye did not influence the PNB generation. The high concentration of the dye in intact liposomes quenched the fluorescence below a detectable level. However, the alcohol-induced destruction of liposomes and the release of the dye in a suspension increased the level of green fluorescence by 1,600%. Free

liposomes and GNPs were washed off of cells before the exposure of the cells to laser pulses. See also Supplementary Methods.

Doxorubicin-loaded liposomes—Standard Doxil liposomes with doxorubicin, a water-soluble drug (Ben Venue Laboratories, Inc, Bedford, OH), were functionalized with the C225 antibody. We incubated the cells with liposomes simultaneously with GNP-C225 for 24 h. We washed the free liposomes and GNPs off of the cells before exposing them to laser pulses.

Paclitaxel-loaded micelles—The paclitaxel-loaded micelles were prepared by the lipid film hydration method. The micelle diameter was 14.5 ± 0.11 nm. They were functionalized with C225 (antibody against EGFR) or 2C5 (antibody against nucleosomes) and incubated with cells and GNP-C225 for 4 h (37 °C). We washed the free micelles and GNPs off of the cells before exposing them to laser pulses. See additional details in Supplementary Methods.

Intracellular aggregation of GNP and TN into a mixed cluster was achieved by activating the universal cell defense, receptor-mediated endocytosis. Cells self-assemble nanoclusters (i) by accumulating nanoparticles at the membrane as a result of the interaction of the nanoparticle-conjugated antibody with EGFR and (ii) through receptor-mediated endocytosis of membrane-bound nanoparticles[8,9,12,42]. As a result (Fig. 3i,j), 5–50 GNPs are aggregated into a cluster in endosomes or lysosomes, and the largest clusters are formed by the most aggressive cancer cells due to the maximal GNP accumulation at the membranes. Due to unavoidable nonspecific uptake, some GNPs and TNs end up in normal cells and tissues (Fig. 3h and Supplementary Fig. 4b,c). Formation of this ‘Trojan horse’ is a key step in quadrapeutics: it does not trigger any therapeutic effect and can remain safe and stable until it is externally activated with a laser pulse and X-rays.

Step 2: local generation and detection of plasmonic nanobubbles

Local generation and detection of plasmonic nanobubbles was achieved with a short near-infrared laser pulse to cause mechanical destruction of target cells and intracellular drug release (Supplementary Fig. 6b).

2.1: PNB generation—A PNB is the localized nonstationary event, an evaporation of liquid around a laser pulse–heated GNP, that results in the transient expansion and collapse of a vapor nanobubble in nanoseconds. The short laser pulse prevents thermal diffusion to the bulk medium[7]. In addition, the emerging vapor further insulates the hot GNP cluster from its bioenvironment[8,9]. Thus, PNB generation is thermally safe and has zero thermal impact. We induced PNBs with a single picosecond laser pulse (PL-2250/2143, Ekspla, Vilnius, Lithuania) at the wavelengths of 532 nm or 780 nm using our new method of nonstationary optical excitation of GNPs[18]. This method uses a single short laser pulse to generate PNBs *in vitro* and *in vivo* with a very high, 2- to 4-nm wide spectral selectivity (Supplementary Fig. 5c), around clinically validated gold colloids[3,4] in the near-infrared spectral region (780 nm), where the tissue transparence is maximal and the depth of optical penetration is up to 10 mm (refs. 19,43,44). PNB diameter and lifetime were controlled via

the pulse fluence (energy per cm^2). The diameter of the excitation laser beam was 220 μm in *in vitro* studies and 470 μm *in vivo*.

2.2: real-time detection of PNBs—Real-time detection of PNBs in individual cells was based on their optical scattering through a time-resolved optical scattering image (Fig. 2b) and a trace (Fig. 2b). We obtained the images with a pulsed probe beam (576 nm, 70 ps, 0.1 mJ cm^{-2}). A PNB image showed the location of the PNB. We measured the maximal diameter of the PNB simultaneously with the optical scattering trace *in vitro* (Fig. 2b) and acoustic trace *in vivo* (Fig. 5a and Supplementary Fig. 5a). An optical trace was obtained by focusing an additional continuous laser beam of very low power (633 nm, 0.05 mW, 05-STP-901, CVI Meller Griot, Albuquerque, NM) on the cells. The PNB-induced scattering of the probe beam decreased its axial intensity, which was monitored with a high-speed photodetector, thus producing a trace of a PNB-specific shape (Fig. 2b). The duration of this trace at half of its maximum was measured as the PNB lifetime, which correlates to the maximal diameter of the PNB[7]. A PNB emits a strong pressure pulse during its expansion and collapse, similar to that of an acoustic emission during cavitation. This broadband pressure pulse was detected *in vivo* remotely through the tissue by using an ultrasound transducer XMS-310 (10 MHz, Olympus NDT Inc., Waltham, MA) with preamplifier (Ultrasonic Preamp 5676, Olympus NDT Inc., Waltham, MA). We assembled all hardware on an inverted optical microscope (Zeiss Axiovert 200) and operated it with a PC through custom software modules developed on a LabView platform (National Instruments Corporation, Austin, TX).

2.3: mechanical destruction of the host cells—Mechanical destruction of the host cells with PNBs (Fig. 3b) employed the disruptive, explosive, mechanical impact of large PNBs with a lifetime of >200 ns. These large PNBs instantaneously destroy the host cancer cells by disrupting their membranes and internal structures in nanoseconds and without any thermal impact[12]. At the same time, the localized nature of a PNB spares even adjacent normal cells. In contrast to the mechanical effect of PNBs, current laser microsurgery and thermal therapy[20,45,46] employ bulk thermal effects that require high optical doses and long exposure times, four to six orders of magnitude higher than those in quadrapeutics, and thus have low cancer cell specificity and often do not prevent tumor recurrence[47]. GNPs improve the efficacy of these photothermal therapies[46] (Nanospectra Biosciences, Inc.; pilot study of AuroLase therapy in refractory and/or recurrent tumors of the head and neck, available from http://clinicaltrials.gov/ct2/show/NCT00848042/, with NLM identifier NCT00848042. Nanospectra Biosciences, Inc.; Efficacy Study of AuroLase Therapy in Subjects With Primary and/or Metastatic Lung Tumors, available from http://clinicaltrials.gov/ct2/show/NCT01679470/, with NLM identifier NCT01679470), but their high doses and nonspecific uptake coupled with thermal diffusion do not improve cancer cell specificity or lower systemic toxicity. In contrast, our new method of PNB generation with a short near-infrared laser pulse[18] allows the combination of clinically validated gold colloids[3,4,40,41] (instead of the less safe, engineered, near-infrared GNPs) with safe, deep-penetrating near-infrared light and reduces the therapeutic optical dose by several orders of magnitude compared to other laser- and GNP-based therapies[46,48–50].

2.4: intracellular ejection (release) of the therapeutic payload from nanocarriers—Intracellular ejection (release) of the therapeutic payload from nanocarriers employed systemically administered GNPs and TNs that are colocalized in one intracellular cluster and the locally administered laser pulse. The mechanical impact of small nonlethal PNBs with a lifetime of 20–70 ns (Fig. 2f), colocalized with TNs, disrupts these nanocarriers and endosomes and ejects the drug into the cytoplasm within nanoseconds only in cancer cells (Fig. 2e,g). This unique release mechanism radically differs from the traditional slow diffusive leak from TNs due to the instantaneous and localized ejection of the drug from TNs. Such a rapid and localized release creates a high concentration of the ejected free drug in the cytoplasm of a cancer cell (Fig. 2g). This high intracellular drug concentration, in turn, overcomes the drug resistance of cancer cells. Compared to standard chemotherapy and chemoradiation therapy (Supplementary Table 1 provides a more detailed comparison), quadrapeutics demonstrates a radical increase in therapeutic efficacy, specificity and safety. The therapeutic efficacy and safety of current targeted therapeutic nanocarriers[51,52] are limited by (i) slow diffusive release mechanisms that 'leak' the drug en route and in cancer cells without creating its high intracellular concentration fast enough[34,53], (ii) significant nonspecific uptake by normal cells due to the high doses of nanocarriers (one to two orders of magnitude higher than those applied in quadrapeutics)[35,36,54] and (iii) the failure to discriminate cancer cells from normal cells when using external energy modalities[28,35,55] alone or in combination with GNPs[48–50], or complex theranostic nanocarriers[49,50]. Some nanocarriers are marketed as 'nanobubbles'[56,57], but, being particles, they have all the limitations of the aforementioned nanocarriers and none of the properties of PNBs. PNBs also differ from macro vapor (cavitation) bubble-based macrotherapies[58], which are not cancer cell–specific and also require high drug doses.

Step 3: amplification of X-rays

Amplification of X-rays (Supplementary Fig. 6c) employed GNP-C225 conjugates administered systemically and a single X-ray dose administered locally after the formation of GNP clusters. GNP clusters amplify external X-rays by emitting local secondary electrons upon absorption of X-rays (Fig. 1c)[14]. The X-ray amplification is limited to several micrometers and is maximal for large GNP clusters, which are located in the most aggressive cancer cells. Likewise, the X-ray is minimally amplified for the single GNPs or their small clusters taken up by normal cells. Thus, the amplification is limited to the host cancer cell and it cannot damage the nearby normal cells. Cells and animals were irradiated with X-rays with a RS 2000 machine (Rad Source Technologies, Inc., Suwanee, GA). For combination treatment, we administered the X-rays 1 to 6 h after the laser treatment. We used a standard irradiation mode (160 kV, 25 mA, with a copper filter). All cells and animals received a single treatment.

These three steps were applied *in vitro* and *in vivo* to the models described below.

Cells

We used HNSCC cells in *in vitro* and *in vivo* studies. We used HN31 line to model aggressive cancer and HN30 line to model indolent cancer[17]. Both cell lines overexpress the epidermal growth factor receptor (EGFR) that was validated in clinic for the treatment of

head and neck cancers (Supplementary Methods). We used normal epithelial human oral kerotinocyte NOM9 in *in vitro* therapeutic studies. The suspension model used other EGFR-negative cells, Jurkat (J32) suspension cell line, because adherent NOM9 cells have a low survival rate after the trypsinization and multiple staining procedures employed in the suspension experiments. We measured pixel image amplitudes of dye-specific fluorescence and optical scattering locally in individual cells for at least 150 cells per sample, by using image cytometry with a laser scanning confocal microscope LSM710 (Carl Zeiss MicroImaging GmbH, Germany). We obtained population-averaged metrics to characterize the drug release (green fluorescence), cell type (red and blue fluorescence), integrity of the PNB-treated cells (Calcein red fluorescence) and GNP uptake (optical scattering). Calcein green excitation/emission/bandpass wavelength: 488/530/25 nm; Calcein red-orange excitation/emission/bandpass wavelength: 543/574/26 nm; DAPI excitation/emission/bandpass wavelength: 405/462/44 nm. Head and neck cell lines were obtained from J. Myers' laboratory, UT MD Anderson Cancer Center (Houston, TX), and the J32 cell line was obtained from L. Metelitsa's laboratory, Texas Children's Hospital (Houston, TX).

Animals

We purchased healthy, male athymic nude mice, age 8 to 12 weeks, from the National Cancer Institute-Frederick Cancer Research and Development Center (Frederick, MD) and used them in accordance with Animal Care Use Guidelines under the protocols approved by the Institutional Animal Care and Use Committee of the University of Texas MD Anderson Cancer Center and Rice University Institutional Animal Care and Use Committee.

Primary tumors—Primary tumors were induced by s.c. injection of a reduced number, 180,000, of the *in vitro* pretreated HN31 cells into the flank of nude mice (Fig. 4a). We analyzed four treatment groups: intact HNSCC cells (five animals), HNSCC cells pretreated with PNBs (without drugs or X-rays) (five animals), HNSCC cells pretreated with standard chemoradiation therapy (Doxil, 2 μg ml^{-1} and X-rays, 4 Gy) (six animals) and HNSCC cells pretreated with quadrapeutics (Doxil, 2 μg ml^{-1}, GNP, 2.4×10^{10} particles ml^{-1}, laser pulse, 45 mJ cm^{-2} at 24 h after GNP administration, X-rays, 4 Gy, 6 h after laser treatment) (four animals). The tumors were characterized by their volume and the incidence rate at the stage (15 d) when the untreated tumors typically reached a moribund condition.

Primary xenograft HNSCC tumors—Primary xenograft HNSCC tumors were induced s.c. by injecting 500,000 luciferase-encoded HN31 or HN30 cells and were grown to 3–5 mm. Tumors were quantified weekly via their volume (measured with a caliper) and luciferase-induced bioluminescence (measured via small animal imaging system IVIS Lumina). One group received no treatment (six animals) and another three groups received the following single primary treatments: quadrapeutic group (11 animals) received GNP-C225s (0.8 μg g^{-1}) and Doxil-C225 (1 mg kg^{-1}) via intravenous concomitant injection. After 24 h, we scanned the tumor areas (15 × 15 mm) with broad near-infrared laser pulses (780 nm, 45 mJ cm^{-2}), and then after 6 h we exposed them to X-rays (4 Gy). The PNB group (four animals) received identical doses of GNP and laser pulses. We monitored the generation of PNBs in the tumors with an ultrasound detector during the laser scan (Fig. 5a). The chemoradiation group (11 animals) received identical doses of drugs and X-rays as the

quadrapeutic group. We monitored all the animals for 3 weeks, the period that stably showed a moribund condition among untreated animals. We measured tumor width and length with digital calipers and calculated the tumor volume in mm^3 as volume = $(width)^2 \times length/2$ (Supplementary Methods). We monitored the animals for 3 weeks after the treatment, and they were euthanized on reaching a moribund condition.

MRD model—We induced tumors in mice with an s.c. injection of human HNSCC HN31 cells (encoded with GFP) into the flanks. Between 14 and 17 d after the cell injections, when the tumors were established (8–10 mm in diameter), we injected GNP-C225 (0.8 μg g^{-1} of body weight) and/or Doxil-C225 (1 mg kg^{-1} of body weight) conjugates into the mice via the tail vein. Twenty-four hours after the GNP and drug injection, we anesthetized the mice, fully resected the tumors and exposed the surgical margins to a scanning laser beam to generate and detect PNBs. The surgical wounds were then closed. We monitored local recurrence of HNSCC in the animals by visual observation and imaging of HNSCC fluorescence with IVIS Lumina. We analyzed the incidence of tumor recurrence and the intensity of GFP fluorescence signals 28 d after the surgery in the three treatment modes: surgery (five animals), surgery with adjuvant chemoradiation therapy (Doxil + X-rays) (six animals) and surgery with adjuvant quadrapeutics (seven animals). See additional details in Supplementary Methods.

Therapeutic efficacy and statistical analyses

The therapeutic effect was measured *in vitro* as short-term viability and long-term clonogenicity as the surviving fraction. Our *in vivo* studies used four to eleven animals in each group. Animal group sizes were set to support a statistically valid data and to minimize the animal use. Animals were randomly assigned to groups for the experiments. The animals studies were not blinded, as the same investigators performed the grouping, dosing and analyses, rendering blinding of the studies unfeasible. We analyzed the *in vivo* therapeutic efficacy using three standard metrics: the tumor incidence rate, tumor volume and the intensity of the fluorescence (or luminescence) of encoded tumor cells. We analyzed the therapeutic amplification *in vitro* by dividing the surviving fraction of chemoradiation-treated cells by that of quadrapeutics-treated cells, and *in vivo* by dividing the volume of chemoradiation-treated animals by that of quadrapeutics-treated animals. We used two-tailed *t*-tests to compare the groups for HNSCC cell fluorescence, tumor incidence and volumes. We performed statistical analyses with Origin software (OriginPro8, OriginLab Corporation, Northampton, MA). *P* values of <0.05 were considered statistically significant.

Supplementary Material

Refer to Web version on PubMed Central for supplementary material.

ACKNOWLEDGMENTS

We thank J. Myers (MD Anderson Cancer Center, NOM9 cell line), L. Metelitsa (Texas Children's Hospital, J32 cell line) and J. Ensley (Wayne State University, HN30 and HN31 cell lines) for sharing cell lines, E. Hanna, A. Gillenwater, H. Skinner and M. Kupferman for helpful discussions of head and neck cancer, G. Peng, R. Bouchard and C. Kingsley for technical help, D.S. Wagner for discussing cellular effects of PNBs, G. Mixon, S. Saunders, D. Grayson and M. Martinez for engineering and administrative help, D. Townley for performing transmission electron microscopy and W. Hartner and S. Parminter for editing. This work was supported by US National

Institutes of Health (NIH) grant R01GM094816, US National Science Foundation grant CBET-1341212 and Virginia and L.E. Simmons Family Foundation Award (D.O.L.), US NIH grants R01CA128486 (V.P.T.), 5U54151881-012 (V.P.T.) and S10RR026399-01 (confocal microscope).

References

1. Meier JD, Oliver DA, Varvares MA. Surgical margin determination in head and neck oncology: current clinical practice. The results of an International American Head and Neck Society Member Survey. Head Neck. 2005; 27:952–958. [PubMed: 16127669]
2. Langendijk JA, et al. Impact of late treatment-related toxicity on quality of life among patients with head and neck cancer treated with radiotherapy. J. Clin. Oncol. 2008; 26:3770–3776. [PubMed: 18669465]
3. Libutti SK, et al. Phase I and pharmacokinetic studies of CYT-6091, a novel PEGylated colloidal gold-rhTNF nanomedicine. Clin. Cancer Res. 2010; 16:6139–6149. [PubMed: 20876255]
4. Kean WF, Kean IR. Clinical pharmacology of gold. Inflammopharmacology. 2008; 16:112–125. [PubMed: 18523733]
5. Sharafinski ME, Ferris RL, Ferrone S, Grandis JR. Epidermal growth factor receptor targeted therapy of squamous cell carcinoma of the head and neck. Head Neck. 2010; 32:1412–1421. [PubMed: 20848399]
6. Iakoubov L, Rokhlin O, Torchilin V. Anti-nuclear autoantibodies of the aged reactive against the surface of tumor but not normal cells. Immunol. Lett. 1995; 47:147–149. [PubMed: 8537094]
7. Lukianova-Hleb E, et al. Plasmonic nanobubbles as transient vapor nanobubbles generated around plasmonic nanoparticles. ACS Nano. 2010; 4:2109–2123. [PubMed: 20307085]
8. Lukianova-Hleb EY, et al. Improved cellular specificity of plasmonic nanobubbles versus nanoparticles in heterogeneous cell systems. PLoS ONE. 2012; 7:e34537. [PubMed: 22509318]
9. Lukianova-Hleb EY, Ren X, Zasadzinski JA, Wu X, Lapotko D. Plasmonic nanobubbles enhance efficacy and selectivity of chemotherapy against drug-resistant cancer cells. Adv. Mater. 2012; 24:3831–3837. [PubMed: 22407874]
10. Koukourakis MI, et al. Liposomal doxorubicin and conventionally fractionated radiotherapy in the treatment of locally advanced non-small-cell lung cancer and head and neck cancer. J. Clin. Oncol. 1999; 17:3512–3521. [PubMed: 10550149]
11. Torchilin VP, Lukyanov AN, Gao Z, Papahadjopoulos-Sternberg B. Immunomicelles: targeted pharmaceutical carriers for poorly soluble drugs. Proc. Natl. Acad. Sci. USA. 2003; 100:6039–6044. [PubMed: 12716967]
12. Wagner DS, et al. The *in vivo* performance of plasmonic nanobubbles as cell theranostic agents in zebrafish hosting prostate cancer xenografts. Biomaterials. 2010; 31:7567–7574. [PubMed: 20630586]
13. Hainfeld JF, et al. Gold nanoparticles enhance the radiation therapy of a murine squamous cell carcinoma. Phys. Med. Biol. 2010; 55:3045–3059. [PubMed: 20463371]
14. Hainfeld JF, Slatkin DN, Smilowitz HM. The use of gold nanoparticles to enhance radiotherapy in mice. Phys. Med. Biol. 2004; 49:N309–N315. [PubMed: 15509078]
15. Calais G, et al. Stage III and IV cancers of the oropharynx: results of a randomized study of Gortec comparing radiotherapy alone with concomitant chemotherapy. Bull. Cancer. 2000; 87:48–53. [PubMed: 11082723]
16. Sano D, et al. Vandetanib restores head and neck squamous cell carcinoma cells' sensitivity to cisplatin and radiation *in vivo* and *in vitro*. Clin. Cancer Res. 2011; 17:1815–1827. [PubMed: 21350000]
17. Sano D, et al. Disruptive TP53 mutation is associated with aggressive disease characteristics in an orthotopic murine model of oral tongue cancer. Clin. Cancer Res. 2011; 17:6658–6670. [PubMed: 21903770]
18. Lukianova-Hleb EY, Volkov AN, Wu X, Lapotko DO. Transient enhancement and spectral narrowing of the photothermal effect of plasmonic nanoparticles under pulsed excitation. Adv. Mater. 2013; 25:772–776. [PubMed: 23161793]

19. Welch, AJ.; van Gemert, MJC. Optical-Thermal Response of Laser-Irradiated Tissue. 2nd edn.. Welch, AJ.; van Gemert, MJC., editors. Springer; 2011. p. 3-11.
20. Ambrosch P. The role of laser microsurgery in the treatment of laryngeal cancer. Curr. Opin. Otolaryngol. Head Neck Surg. 2007; 15:82–88. [PubMed: 17413407]
21. Karni RJ, Rich JT, Sinha P, Haughey BH. Transoral laser microsurgery: a new approach for unknown primaries of the head and neck. Laryngoscope. 2011; 121:1194–1201. [PubMed: 21495044]
22. Lukianova-Hleb EY, Lapotko D. Influence of transient environmental photothermal effects on optical scattering by gold nanoparticles. Nano Lett. 2009; 9:2160–2166. [PubMed: 19374436]
23. Rahman WN, et al. Enhancement of radiation effects by gold nanoparticles for superficial radiation therapy. Nanomedicine. 2009; 5:136–142. [PubMed: 19480049]
24. Jiao P, et al. Leading neuroblastoma cells to die by multiple premeditated attacks from a multifunctionalized nanoconstruct. J. Am. Chem. Soc. 2011; 133:13918–13921. [PubMed: 21827210]
25. Argiris A, Karamouzis MV, Raben D, Ferris RL. Head and neck cancer. Lancet. 2008; 371:1695–1709. [PubMed: 18486742]
26. Jegannathen A, et al. Synchronous chemoradiotherapy in patients with locally advanced squamous cell carcinoma of the head and neck using capecitabine: a single-centre, open-label, single-group phase II study. Clin. Oncol. (R Coll Radiol). 2011; 23:149–158. [PubMed: 20951012]
27. Chen Y, et al. Phase I/II clinical study of pulsed paclitaxel radiosensitization for thoracic malignancy a therapeutic approach on the basis of preclinical research of human cancer cell lines. Clin. Cancer Res. 2003; 9:969–975. [PubMed: 12631594]
28. Paliwal S, Mitragotri S. Ultrasound-induced cavitation: applications in drug and gene delivery. Expert Opin. Drug Deliv. 2006; 3:713–726. [PubMed: 17076594]
29. Czarnota GJ, et al. Tumor radiation response enhancement by acoustical stimulation of the vasculature. Proc. Natl. Acad. Sci. USA. 2012; 109:E2033–E2041. [PubMed: 22778441]
30. Rapoport N, et al. Ultrasound-mediated tumor imaging and nanotherapy using drug loaded, block copolymer stabilized perfluorocarbon nanoemulsions. J. Control. Release. 2011; 153:4–15. [PubMed: 21277919]
31. Gao Z, Kennedy AM, Christensen DA, Rapoport NY. Drug-loaded nano/microbubbles for combining ultrasonography and targeted chemotherapy. Ultrasonics. 2008; 48:260–270. [PubMed: 18096196]
32. Rapoport N. Physical stimuli-responsive polymeric micelles for anti-cancer drug delivery. Prog. Polym. Sci. 2007; 32:962–990.
33. Rapoport NY, Gao Z, Kamaev P, Christensen DA. Ultrasound-enhanced localized chemotherapy of drug-sensitive and multidrug resistant tumors. AIP Conf. Proc. 2006; 829:481.
34. Allen TM, Cullis PR. Drug delivery systems: entering the mainstream. Science. 2004; 303:1818–1822. [PubMed: 15031496]
35. Schroeder A, et al. Treating metastatic cancer with nanotechnology. Nat. Rev. Cancer. 2011; 12:39–50. [PubMed: 22193407]
36. Peer D, et al. Nanocarriers as an emerging platform for cancer therapy. Nat. Nanotechnol. 2007; 2:751–760. [PubMed: 18654426]
37. de Carvalho AC, et al. Clinical significance of molecular alterations in histologically negative surgical margins of head and neck cancer patients. Oral Oncol. 2012; 48:240–248. [PubMed: 22104250]
38. Zhang HF, Maslov K, Stoica G, Wang LV. Functional photoacoustic microscopy for high-resolution and noninvasive *in vivo* imaging. Nat. Biotechnol. 2006; 24:848–851. [PubMed: 16823374]
39. Qian X, et al. *In vivo* tumor targeting and spectroscopic detection with surface-enhanced Raman nanoparticle tags. Nat. Biotechnol. 2008; 26:83–90. [PubMed: 18157119]
40. Merchant B. Gold, the noble metal and the paradoxes of its toxicology. Biologicals. 1998; 26:49–59. [PubMed: 9637749]

41. Root SW, Andrews GA, Kniseley RM, Tyor MP. The distribution and radiation effects of intravenously administered colloidal gold-198 in man. Cancer. 1954; 7:856–866. [PubMed: 13199762]
42. Lapotko DO, Lukianova-Hleb E, Oraevsky A. Clusterization of nanoparticles during their interaction with living cells. Nanomedicine. 2007; 2:241–253. [PubMed: 17716124]
43. Weissleder R. A clearer vision for *in vivo* imaging. Nat. Biotechnol. 2001; 19:316–317. [PubMed: 11283581]
44. Qian X, et al. *In vivo* tumor targeting and spectroscopic detection with surface-enhanced Raman nanoparticle tags. Nat. Biotechnol. 2008; 26:83–90. [PubMed: 18157119]
45. Vogl TJ, Naguib NN, Lehnert T, Nour-Eldin NE. Radiofrequency, microwave and laser ablation of pulmonary neoplasms: clinical studies and technical considerations-review article. Eur. J. Radiol. 2011; 77:346–357. [PubMed: 19700254]
46. O'Neal DP, Hirsch LR, Halas NJ, Payne JD, West JL. Photo-thermal tumor ablation in mice using near infrared-absorbing nanoparticles. Cancer Lett. 2004; 209:171–176. [PubMed: 15159019]
47. Roedel RM, et al. Transoral laser microsurgery for recurrence after primary radiotherapy of early glottic cancer. Auris Nasus Larynx. 2010; 37:474–481. [PubMed: 20031355]
48. Agarwal A, MacKey MA, El-Sayed MA, Bellamkonda RV. Remote triggered release of doxorubicin in tumors by synergistic application of thermosensitive liposomes and gold nanorods. ACS Nano. 2011; 5:4919–4926. [PubMed: 21591812]
49. Braun GB, et al. Laser-activated gene silencing via gold nanoshell-siRNA conjugates. ACS Nano. 2009; 3:2007–2015. [PubMed: 19527019]
50. Park JH, et al. Cooperative nanoparticles for tumor detection and photothermally triggered drug delivery. Adv. Mater. 2010; 22:880–885. [PubMed: 20217810]
51. O'Neill BE, Rapoport N. Phase-shift, stimuli-responsive drug carriers for targeted drug delivery. Ther. Deliv. 2011; 2:1165–1187. [PubMed: 22059114]
52. Rapoport N, Gao Z, Kennedy A. Multifunctional nanoparticles for combining ultrasonic tumor imaging and targeted chemotherapy. J. Natl. Cancer Inst. 2007; 99:1095–1106. [PubMed: 17623798]
53. Panyam J, Labhasetwar V. Biodegradable nanoparticles for drug and gene delivery to cells and tissue. Adv. Drug Deliv. Rev. 2003; 55:329–347. [PubMed: 12628320]
54. Kamaly N, et al. Targeted polymeric therapeutic nanoparticles: design, development and clinical translation. Chem. Soc. Rev. 2012; 41:2971–3010. [PubMed: 22388185]
55. Qiu Y, Park K. Environment-sensitive hydrogels for drug delivery. Adv. Drug Deliv. Rev. 2001; 53:321–339. [PubMed: 11744175]
56. Ferrara KW. Driving delivery vehicles with ultrasound. Adv. Drug Deliv. Rev. 2008; 60:1097–1102. [PubMed: 18479775]
57. Rapoport NY, Kennedy AM, Shea JE, Scaife CL, Nam KH. Controlled and targeted tumor chemotherapy by ultrasound-activated nanoemulsions/microbubbles. J. Control. Release. 2009; 138:268–276. [PubMed: 19477208]
58. Kennedy JE. High-intensity focused ultrasound in the treatment of solid tumours. Nat. Rev. Cancer. 2005; 5:321–327. [PubMed: 15776004]

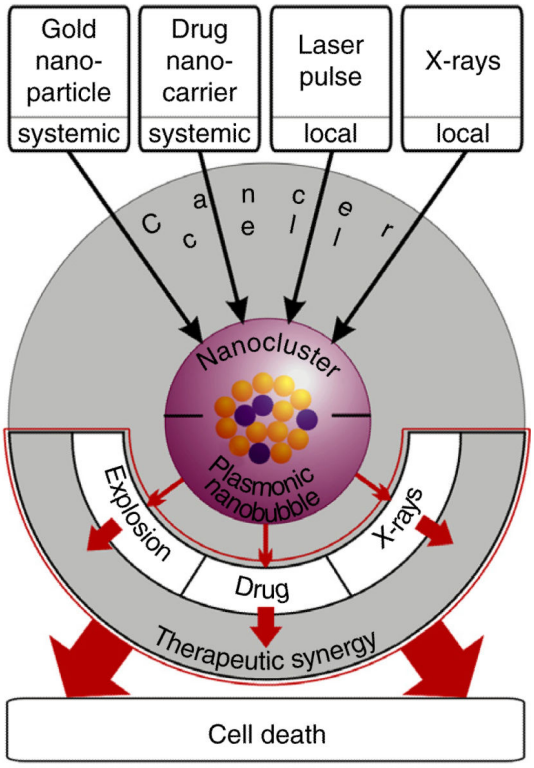

Figure 1.

Principle of the quadrapeutics: four components—colloidal gold, encapsulated drugs, low-energy short laser pulses and X-rays—are administered in a simple three-step protocol. First, cancer cells self-assemble antibody-functionalized gold nanoparticles and drug-loaded nanocarriers into intracellular nanoclusters via receptor-mediated endocytosis. Second, the on-demand threshold activation of these nanoclusters with an external laser pulse and X-rays triggers colocalized intracellular transient events: mechanical explosion of vapor PNBs, instantaneous ejection of drugs into cytoplasm and local amplification of X-rays. The intracellular synergy of these three threshold-activated, mechanical and physical events selectively amplifies the therapeutic effect of standard chemotherapy and chemoradiation only in cancer cells.

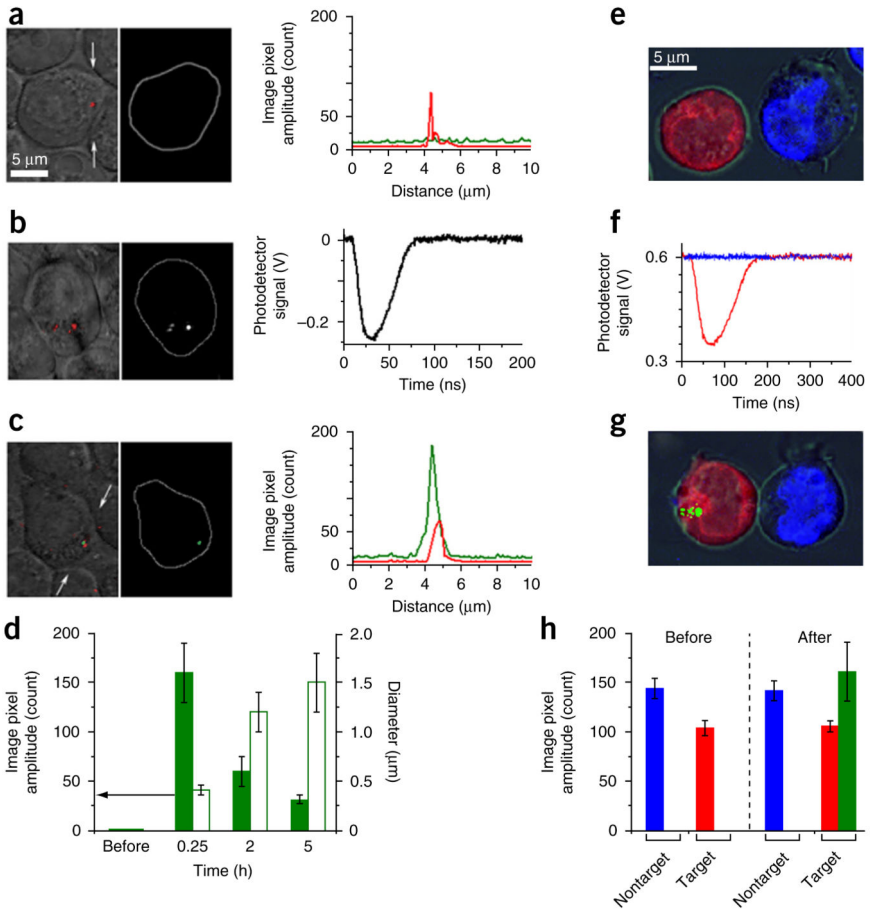

Figure 2.

PNB-enhanced intracellular on-demand ejection (release) of encapsulated calcein green dye. (**a**–**c**) Confocal microscopy images of living cells treated with green fluorescent dye–loaded liposomes conjugated with 2C5 antibody (detected as green in fluorescent mode) and GNP-C225 conjugates (detected as red in scattering mode). (**a**) Before the laser pulse, green fluorescence is quenched and dimmed in intact liposomes. (**b**) During the laser pulse, clusters of GNPs (left) following exposure to a single picosecond laser pulse (532 nm, 40 mJ cm^{-2}) generate colocalized PNBs (center, optical scattering time-resolved image) that are quantified through their optical scattering trace (right). (**c**) Immediately after a single laser pulse, green fluorescence coincides with GNP cluster and PNB. (**d**) Cell population–averaged kinetics of image pixel amplitude of green fluorescence (solid) and size of fluorescent zone (open) in individual cells before and after the laser pulse. (**e**) Cellular specificity of PNB-enhanced intracellular dye release. Merged brightfield and confocal tricolor fluorescent image of coculture of EGFR-positive (red) and EGFR-negative (blue) cells treated with conjugates of GNPs and liposomal green dye (dimmed owing to the fluorescence quenching in intact liposomes). (**f**) Optical scattering traces show the selective generation of PNBs only in red EGFR-positive cancer cells following simultaneous exposure of all cells to a single broad laser pulse (532 nm, 40 mJ cm^{-2}, red trace for EGFR-positive cell and blue trace for EGFR-negative cell). (g) Cells at 5–10 min after exposure to a single laser pulse show the localized release of green dye only in EGFR-positive cell

owing to the selective generation of small PNB that disrupted the dye nanocarriers and endosome and locally ejected the dye (green). Nonspecific uptake of GNPs in EGFR-negative cell did not generate PNBs and thus did not trigger the dye release. (**h**) Cell population-averaged image pixel amplitudes of EGFR-positive (red) and EGFR-negative (blue) individual cells before and after their exposure to a single laser pulse and the corresponding levels of calcein green fluorescence in individual cells (green); $n = 150$ for each experimental group for **d** and **h**. The images in **a**–**g** are representative of three independent experiments. Data are expressed as mean ± s.d.

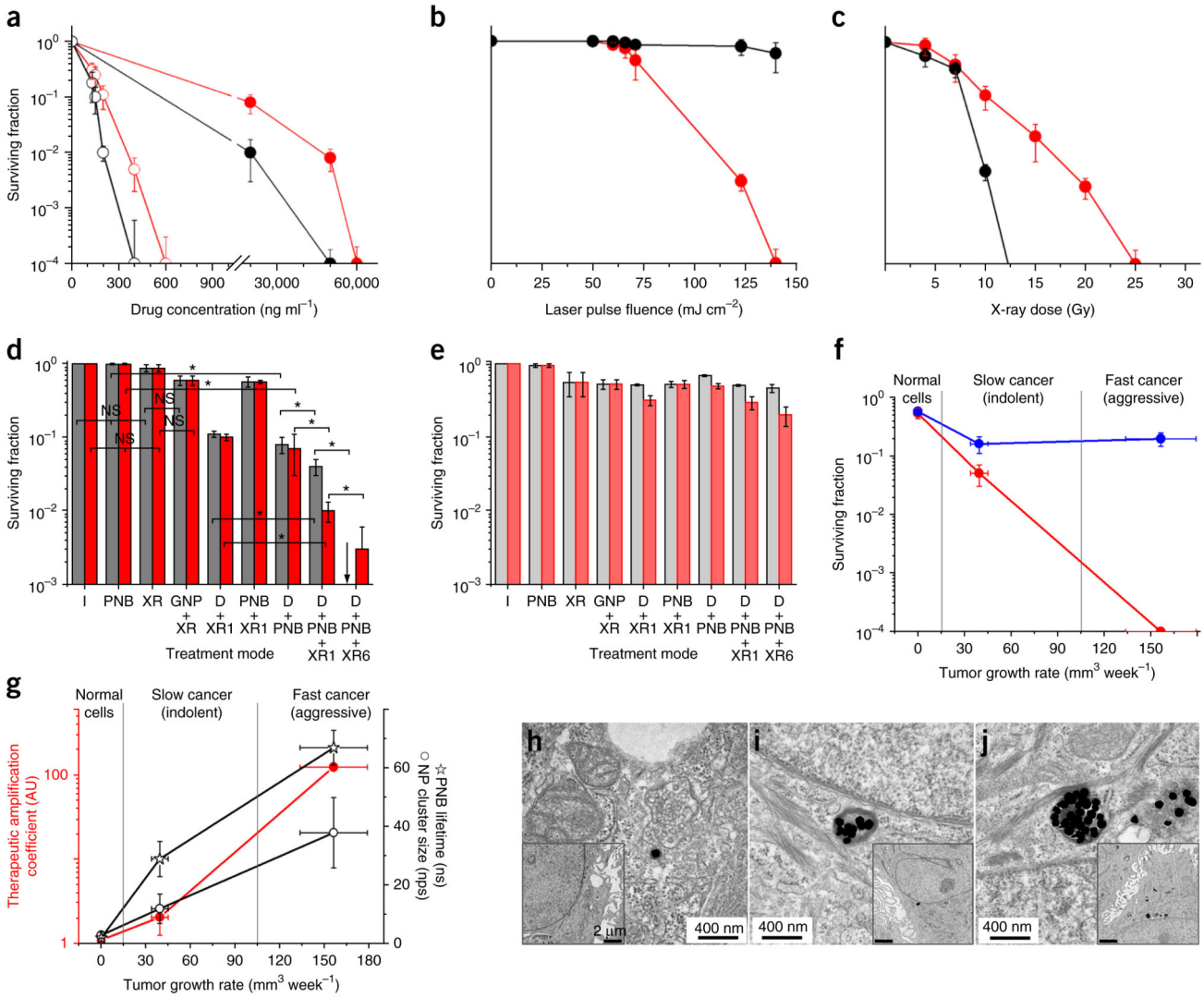

Figure 3.

Quadrapeutics mechanisms *in vitro*. (**a**–**c**) Surviving fraction of cancer HN31 cells (red circles) and normal NOM9 cells (black circles) in response to single therapeutic agents as function of drug concentration (Doxil, solid circles; micellar paclitaxel, open circles) (**a**), PNB via the laser pulse fluence (n = 3) (**b**) and X-ray dose (n = 3) (**c**). (**d,e**) Surviving fraction of cancer HN31 (**d**) and normal NOM9 (**e**) cells as a function of the treatment mode for Doxil (gray) and paclitaxel (red). I, intact cells; PNB, GNP-C225 conjugates and single laser pulse (780 nm, 45 mJ cm^{-2}); XR, X-rays, 4 Gy; GNP + XR, GNP-C225 and X-rays; D + XR1, drug (Doxil, 2 μg ml^{-1}; paclitaxel, 33 ng ml^{-1}) and X-rays (chemoradiation); PNB + XR1, GNP-C225, single laser pulse and X-rays 1 h after laser exposure; D + PNB, GNP-C225, drug and laser pulse; D + PNB + XR1, GNP-C225, drug, laser pulse and X-rays 1 h after laser exposure (quadrapeutics); D + PNB + XR6, GNP-C225, drug, laser pulse and X-rays 6 h after laser exposure (quadrapeutics). Black arrow indicates a 0 surviving fraction. n = 6 for **d** and **e**. (**f**) Surviving fraction for normal (NOM9), slow-growing indolent cancer (HN30) and fast-growing aggressive cancer (HN31) cells after standard chemoradiation

(blue) and quadrapeutics (red) treatments measured as function of the cancer aggressiveness (characterized via the growth rate of mouse-xenografted tumors for specific cancer cell lines), with all therapeutic doses as in **d**. (g) Therapeutic amplification coefficient (ratio of the surviving fraction of chemoradiation-treated cells to that of quadrapeutics-treated cells, red), population-averaged nanocluster size (measured via the number of nanoparticles (nps) in a cluster) and maximal size of PNB (measured via the PNB lifetime in ns) in normal (NOM9), slow-growing indolent cancer (HN30) and fast-growing aggressive cancer (HN31) cells measured as function of the cancer aggressiveness (characterized via the growth rate of mouse-xenografted tumors for specific cancer cell lines), with all therapeutic doses as in **d**. (**h**–**j**) Transmission electron microscopy images of GNPs and their clusters in cells after 24-h incubation with GNP-C225 for normal NOM9 cells (**h**), indolent cancer HN30 cells (**i**) and aggressive cancer HN31 cells (**j**); insets show the same cells under low magnification (the images in **h**–**j** are representative of three independent experiments). $n = 6$ (for **f** and **g**). Data are expressed as mean ± s.d. for the three independent experiments, $*P < 0.05$, as determined by two-tailed Student's *t*-test. NS, not significant.

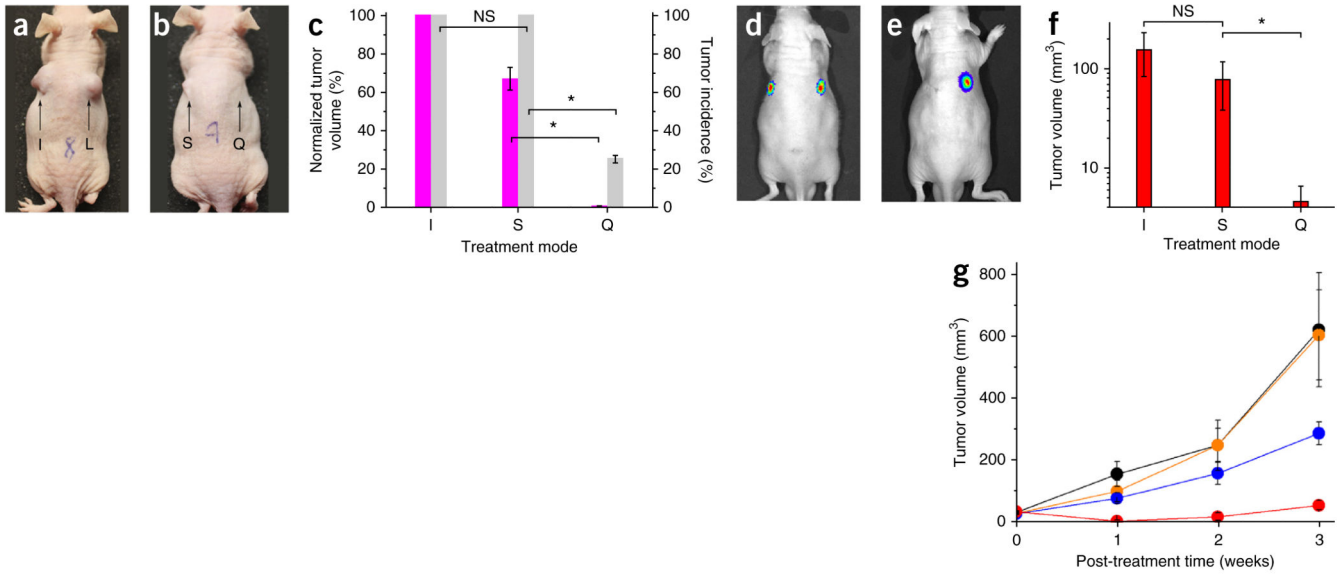

Figure 4.

Quadrapeutics treatment of HNSCC in mouse models. (**a**–**c**) *In vitro*-pretreated HN31 cells injected into mice. (**a,b**) Images of the animals 15 d after the cell injection. I, intact HN31 cells (n = 5); S, chemoradiation therapy-treated cells (n = 6); L, PNB-treated cells (n = 5); Q, quadrapeutics-treated cells (n = 4) (Doxil, 2 μg ml^{-1}; GNP-C225, 2.4 × 10^{10} particles ml^{-1}; laser pulse, 780 nm, 45 mJ cm^{-2}; and X-rays, 4 Gy). (**c**) Tumor incidence rate (gray) and volumes (magenta) in three treatment groups measured 15 d after the cell injection. Data are expressed as mean ± s.e.m. for independent experiments (I, n = 5; S, n = 6; Q, n = 4). (**d**–**g**) Primary tumor model, with bioluminescent images of the animal before (**d**) and 1 week after (e) single-time treatments with quadrapeutics (left flank; Doxil-C225, 1 mg kg^{-1} and GNP-C225, 0.8 mg kg^{-1}, both intravenously injected; laser pulse, 780 nm, 45 mJ cm^{-2}, local; and X-rays, 4 Gy, local (n = 11)) and chemoradiation (right flank, the same doses of Doxil and X-rays (n = 11)). (**f**) Tumor volumes 1 week after the treatment (I, n = 6; S, n = 11; Q, n = 11). (**g**) Time course of the primary tumor volumes after the single-time *in vivo* administration of the following treatments: quadrapeutics (Doxil-C225, 1 mg kg^{-1}; GNP-C225, 0.8 mg kg^{-1}; laser pulse, 780 nm, 45 mJ cm^{-2}; and X-rays, 4 Gy,), red (n = 11); chemoradiation (identical to the above drug and X-ray dose), blue (n = 11); PNB alone (identical to the above GNP and laser doses), orange (n = 4); and untreated animals, black (n = 6). Data are expressed as mean ± s.e.m. *P < 0.05, as determined by two-tailed Student's t-test.

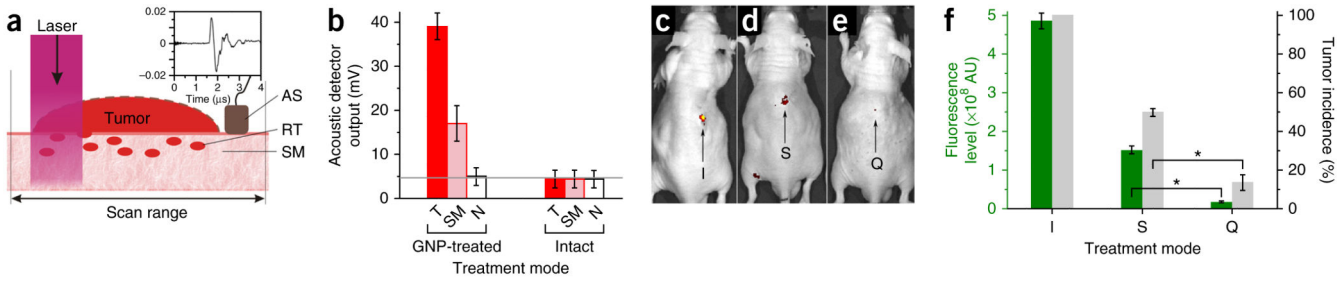

Figure 5.

Evaluation of quadrapeutics for intraoperative real-time diagnosis and treatment of HNSCC MRD. (**a**) Experimental model of intraoperative diagnosis and treatment of MRD. Primary tumor (tumor), residual microtumor (RT) in surgical margins (SM), laser beam scan range and PNB detection with acoustic sensor (AS) and acoustic trace of the PNB (inset). (**b**) Intraoperative diagnosis of MRD. Amplitudes of the PNB acoustic traces obtained during the laser scans in GNP-treated and untreated animals for primary tumors before their resection (T, red), surgical margins immediately after the tumor resection (pink) and adjacent normal tissue (N, white); horizontal gray line shows the background level of acoustic signal. Data are expressed as mean ± s.e.m. (n = 3). (**c**–**e**) Intraoperative treatment of MRD. Fluorescent images of GFP-encoded tumors obtained 28 d after surgery alone (I, n = 5) (**c**), surgery and adjuvant chemoradiation (S, n = 6) (**d**) or surgery and adjuvant quadrapeutics (Q, n = 7) (**e**) (all therapeutic doses identical to those shown in Fig. 4). (**f**) Metrics of recurrent tumors obtained in 28 d after the intraoperative treatment of MRD. Green, level of the tumor fluorescence; gray, incidence rate of a recurrence tumor (I, n = 5; S, n = 6; Q, n = 7). Data are expressed as mean ± s.e.m. *P < 0.05, as determined by two-tailed Student's t-test.